

## High atom utility of robust Ca-Co bimetallic catalyst for efficient Fenton-like catalysis in advanced oxidation processes



Xuanzhi Mao<sup>a,b</sup>, Minglei Wang<sup>a,c,d,\*</sup>, Ji Li<sup>a</sup>, Maojiang Zhang<sup>f</sup>, Chunlei Dong<sup>a,f</sup>, Heng Lei<sup>a,e</sup>, Yulong He<sup>a</sup>, Mingxing Zhang<sup>a</sup>, Zhiqing Ge<sup>g</sup>, Rongfang Shen<sup>a</sup>, Hongwei Han<sup>a</sup>, Jiangtao Hu<sup>a,\*\*</sup>, Guozhong Wu<sup>a,e,\*</sup>

<sup>a</sup> Shanghai Institute of Applied Physics, Chinese Academy of Sciences, No. 2019 Jialuo Road, Jiading, Shanghai 201800, PR China

<sup>b</sup> University of Chinese Academy of Sciences, Beijing 100049, PR China

<sup>c</sup> Institute of Environmental Engineering, ETH Zurich, Zurich 8093, Switzerland

<sup>d</sup> Advanced Analytical Technologies, Swiss Federal Laboratories for Materials Science and Technology (Empa), Ueberlandstrasse 129, Dübendorf 8600, Switzerland

<sup>e</sup> School of Physical Science and Technology, ShanghaiTech University, Shanghai 200031, PR China

<sup>f</sup> College of Materials and Environmental Engineering, Chizhou University, Chizhou, Anhui 247000, PR China

<sup>g</sup> CAS Key Laboratory of Soft Matter Chemistry, Department of Polymer Science and Engineering, University of Science and Technology of China, Hefei, Anhui 230026, PR China

### ARTICLE INFO

#### Keywords:

Radiation-induced graft polymerization

Advanced oxidation process

Bimetallic catalyst

Catalytic mechanism

### ABSTRACT

A durable catalyst composed of Ca-Co bimetallic complex structures on a large-scale substrate was fabricated for efficient activation of peroxyomonosulfate (PMS) in organic pollutant degradation. Specifically, amidoxime groups were introduced onto the polymer substrate via radiation-induced graft polymerization (RIGP), followed by selective adsorption of  $\text{Ca}^{2+}$  and  $\text{Co}^{2+}$  ions. The catalyst demonstrated high effectiveness and stability in degrading 10 mg/L of tetracycline hydrochloride within 8 min by activating PMS under a broad pH range of 3–9. Structural characterization and density functional theory (DFT) calculations confirmed the precise doping of  $\text{Ca}^{2+}$ , which regulated the energy level and enhanced the dispersion of  $\text{Co}^{2+}$ . The combination of bulk substrates and fine structural control in catalytic process provided new ideas for the design of similar catalysts.

### 1. Introduction

Antibiotic pollution in water is a global environmental issue that can cause significant harm to natural ecosystems, even at low concentrations. [1,2]. Studies have explored various treatment processes to eliminate antibiotics from water, including adsorption, membrane separation, biodegradation, coagulation, and advanced oxidation processes (AOPs) [3,4]. AOPs are prominent emerging processes, using hydroxyl ( $\cdot\text{OH}$ ) and sulfate ( $\text{SO}_4^{\cdot-}$ ) radicals, and singlet oxygen ( ${}^1\text{O}_2$ ), and have received extensive attention because of their non-selective degradation and high practical applicability [5–7]. Compared with OH-based Fenton reactions, persulfate-based AOPs have many merits including longer half-time periods, broader working pH ranges and higher redox potentials [8,9]. Thus, water purification processes involving persulfate have generated considerable interest.

In practical application, activation toward peroxyomonosulfate (PMS)

is necessary owing to its sluggish self-decomposition. While many approaches have been established to active PMS, including  $\gamma$ -ray irradiation, ultrasound, and heat, activation by metallic catalysts is considered as the most effective way [10–14]. Ann et al. tested many different metals, including noble metals, and divalent cobalt ions were confirmed as the most effective non-noble metal for activating PMS [15]. However, cobalt ions must be firmly anchored on recyclable substrates, as metallic contamination may result from incomplete recovery of them. Materials such as ultra-small cluster and single-atom site catalysts have been used as ion immobilization matrices to improve the catalytic ability and high atom-utilization efficiency [16–19]. However, these high-activity catalysts are generally expensive and complex to fabricate, requiring precise and rigorous high-temperature pyrolysis processes. Meanwhile, these catalysts are generally micron- or nano-sized and have a tendency to aggregate, which diminishes the catalytic activity. More importantly, separation and recycling of the solution-based media is still a serious

\* Corresponding authors at: Shanghai Institute of Applied Physics, Chinese Academy of Sciences, No. 2019 Jialuo Road, Jiading, Shanghai 201800, PR China.

\*\* Corresponding author.

E-mail addresses: [wangminglei@sinap.ac.cn](mailto:wangminglei@sinap.ac.cn) (M. Wang), [hujiangtao@sinap.ac.cn](mailto:hujiangtao@sinap.ac.cn) (J. Hu), [wuguozhong@sinap.ac.cn](mailto:wuguozhong@sinap.ac.cn) (G. Wu).

problem that severely restricts their practical application. Thus, the preparation of large-scale (meter-scale) catalysts with high specific surface areas, high-density catalytic sites, adequate activities, and stabilities remains a formidable challenge.

Traditional polymer fiber materials, which are affordable, practical, and commercially available, were used to solve the problems of size and cost [20–22]. They have sufficient specific surface area to serve as an appropriate substrate for cobalt-based catalysts, and they can be easily fabricated in an appropriate size and shape while retaining flexibility and strength. Over the past decade, catalyst-loaded fibers have been prepared via various novel process such as electrospinning, melt spinning, and surface coating [23,24]. However, these functional fibers display poor catalytic efficiency and durability because of the entrapment of polymer and the lack of strong interfacial adhesion between catalyst and substrate. In view of the problems encountered in the preparation of efficient and large-scale catalytic materials, we propose a simple process with a potentially broad, and perhaps, “universal” scope to introduce monoatom like catalytic center onto the surface of fibers via radiation-induced graft polymerization (RIGP) techniques and conventional chemical modification. For example, Liu et al. combined cobalt ions with polyethylene terephthalate nonwoven fabric to efficiently activate PMS [25]. Wang et al. used Prussian blue analogues to improve the combining structure between cobalt ions and nonwoven fabric [26]. Mu et al. thoroughly calculated the promotion effect of the chelate structure on the iron ion catalyst. These results highlight the tremendous potential utility of this methodology because these catalysts are cheap and easy to obtain while still being efficient, stable, and recyclable [27]. However, this approach has some disadvantages. The ionic catalytic centers are loaded onto the fiber surface through complexation reactions, which may occupy most of the ions' orbitals, thereby inhibiting their catalytic activity. In addition, it is difficult to enhance the catalyst activity of ion catalysis center by doping with different atoms. Thus, this process achieves the convenience of utility but loses the advantages of common catalysts that can be modified by doping with different elements. Hence, more extensive research is required to enhance the catalytic performance and practicality of such materials.

Herein, we attempted to combine the convenience of large-scale materials and the high catalytic activity of ionic catalytic centers, achieving in-situ doping; the preparation process is provided in Scheme 1. The basic technical method used a widely available polymer substrate and an easy adsorption process. In detail, the graft chains containing amidoxime groups were attached onto the surface of the fiber and then calcium ions were precisely “doped” to cobalt ions achieving atom-level structural control through precise molecular engineering. The resulting calcium-cobalt synergistic catalytic materials exhibit the combined advantages of both elements, leading to improved catalytic performance and stability. This new binary catalyst was denoted as P-PCaCo, and the structural design of it is based on the following considerations. Amidoxime groups were selected as the chelating group because they could offer multiple different adsorption sites, and have large conjugated structures that can enhance chemical activity. Furthermore, in an aqueous medium, the grafted chains extend from a coiled to a stretched

state when chelated with metal ions, which exposes sites and reducing the space distance between active sites, reactive oxygen species (ROS) and organic contaminants, resulting in the high atom-utilization efficiency and dispersion of metal ions. Notably, amidoxime groups can prevent cobalt ions from agglomerating, as excessive chelation simultaneously poisons them. Calcium ions were chosen as the dopant atoms because of the following characteristics. First, and most importantly, the calcium ions can be chelated by the same complexing groups as cobalt ions, with a negligible effect on cobalt adsorption. In detail, calcium ions strongly favor oxygen over nitrogen for complexation, in contrast to cobalt ions, and form the expected complex structure. Second, calcium ions can prevent the aggregation of cobalt ions and simultaneously modulate the electronic structure of the catalytic center by forming a conjugated structure with the cobalt ions, thus enhancing the chemical activity. Finally, the positive charges on the calcium ions might help in capturing PMS, which increases the reaction rate. The catalytic activity of this new high-efficiency catalyst was evaluated by monitoring the aqueous degradation of tetracycline hydrochloride (TC). In addition, the catalyst was further tested under various conditions and systems, to demonstrate its reliability and universality. The morphology and chemical structure of P-PCaCo were elucidated using structural characterization. Electron paramagnetic resonance (EPR) and scavenging radical experiments were used to determine the active species during the catalytic process. X-ray absorption fine structure spectroscopy (XAFS) and density functional theory (DFT) calculations illustrated the detailed catalytic process and the reason for its high efficiency. P-PCaCo provides a new practical method for wastewater treatment, but additional development is required for pilot-scale production.

## 2. Experimental section

### 2.1. Materials

Polyethylene/polyethylene terephthalate nonwoven fabric (PE/PET NWF, S0303) was purchased from SR Commerce Co. Ltd (Japan). Tap water was obtained from Shanghai Institute of Applied Physics, Chinese Academy of Sciences, and waste water was obtained from Tongcheng Yiyuan Water Co., Ltd (China, Anhui). Acrylonitrile (AN), dimethylformamide (DMF), hydroxylamine hydrochloride ( $\text{NH}_2\text{OH}\cdot\text{HCl}$ ), sodium carbonate ( $\text{Na}_2\text{CO}_3$ ), dimethyl sulfoxide (DMSO), cobalt chloride hexahydrate ( $\text{CoCl}_3\cdot 6\text{H}_2\text{O}$ ), calcium chloride ( $\text{CaCl}_2$ ), methyl alcohol ( $\text{MeOH}$ ), tert-butyl alcohol (TBA), potassium dihydrogen phosphate ( $\text{KH}_2\text{PO}_4$ ), potassium chloride (KCl), potassium bicarbonate ( $\text{KHCO}_3$ ), rhodamine B (RhB), methylene blue (MB), ofloxacin (OFX) and sulfathiazole (STZ) were obtained from Sinopharm Chemical Reagent Co., Ltd. (China), peroxyomonosulfate ( $\text{KHSO}_5\cdot 0.5\text{KHSO}_4\cdot 0.5\text{KSO}_4$ , PMS), tetracycline hydrochloride (TH), L-histidine, 5,5-dimethyl-1-pyrrolidine (DMPO), 2,2,6,6-tetramethyl-4-piperidone (TEMP) and metronidazole (MN) were purchased from Sigma-Aldrich. All of them were used as received.



**Scheme 1.** Schematic fabrication process of P-PCaCo.

## 2.2. Fabrication of P-PCaCo

After washed by detergent three times and dried, PE/PET fabrics were laid flat in a plastic bag and then irradiated by electron beam at an absorbed dose rate of 625 Gy/s for 80 s with a total dose of 50 kGy. The energy of electron beam flow is 1.5 MeV with a power of 80 kW while intensity of electron beam is 1.4 mA. After pre-irradiation, fabrics of 5% mass volume fraction was placed in a three-necked flask containing a 20:80 vol% AN:DMF solution with constantly bubbling high purity nitrogen. The graft polymerization reaction took place at 60 °C and finished in three hours. After that, the fabrics named P-PAN was washed by DMF three times and dried to remove residual monomers and homopolymers. The degree of grafting (DG) was calculated by Eq. (1) as follows:

$$\text{DG (\%)} = (W_1 - W_0)/W_0 \times 100\% \quad (1)$$

Where  $W_1$  and  $W_0$  represent weights of P-PAN and PE/PET fabric respectively. Here, DG of this experiment is approximately 81.1%.

Then, 5% mass volume fraction of NH<sub>2</sub>OH-HCl was dissolved in a 50/50 vol% water/DMSO solution, and pH was adjusted to 7 with Na<sub>2</sub>CO<sub>3</sub>. P-PAN of 1% mass volume fraction was immersed in solutions for 4 h at 70 °C. After washed by deionized water and dried, obtained fabrics were denoted as P-PAO.

Finally, 0.5% P-PAO was submerged in different molar ratios of Ca/Co solutions with 1 mol/L total metal ions concentration for 24 h. Shaking repeatedly could result in near-equilibrium adsorption. Obtained fabrics were washed by deionized water three times and dried. Final product was reddish brown and denoted as P-PCaCo.

## 2.3. Characterization

The morphology and elemental distributions of corresponding samples was done by a field emission scanning electron microscope (SEM, FEI Quanta-250, USA) with an energy dispersive spectrometer (EDS). Attenuated total reflection infrared spectra (ATR-IR) was characterized by a Bruker Tensor 207 Fourier-transform infrared spectrometer at a range of 4000–400 cm<sup>-1</sup> with a resolution of 4 cm<sup>-1</sup>. The X-ray photoelectron spectroscopy (XPS) was studied by PHI-5702 electron spectrometer using an Al K $\alpha$  line excitation source with the C 1 s at 285.0 eV as a reference. The capacity of metal ions was quantified by an inductively coupled plasma-atomic emission spectrometry (ICP-OES, Optima 8000, PerkinElmer). Crystallization conditions of materials was analyzed by an X-ray diffraction spectrum (RIGAKU D/MAX2200) using Cu K $\alpha$  radiation ( $k = 1.54 \text{ \AA}$ ). An ultraviolet-visible spectrophotometer (UV-2600, Shimadzu) was utilized to detect absorption spectra from 1000 to 200 nm. The high performance liquid chromatography (HPLC, Agilent 1260-VWD) tests were also analyzed. An electron paramagnetic resonance (EPR) analyzer (Bruker A320, USA) was used to search the EPR spectra by using 5,5-Dimethyl-1-pyrroline-N-oxide (DMPO) and 2,2,6,6-tetramethyl-4-piperidone (TEMP) as spin-trapping agent for the reactive oxygen species. Reaction condition: DMPO = 4  $\mu\text{L}$ , TEMP = 1  $\mu\text{L}$ , H<sub>2</sub>O = 200  $\mu\text{L}$ , [catalyst dosage] = 0.01 g/L, [PMS] = 0.2 g/L, T = 298 K. The total organic carbon (TOC) of the solution was monitored by a TOC analyzer (Analytik Jena AG).

Co K-edge XAFS were tested at BL14W1 station in Shanghai Synchrotron Radiation Facility (SSRF) [28]. The electron storage ring of SSRF was operated at 3.5 GeV, and the maximum current of it was 250 mA. The data was collected by a fixed-exit Si (111) double-crystal monochromator, and the energy was calibrated by metal foils. Obtained EXAFS data was carried out, using the ATHENA module of the IFEFFIT software packages, according to the standard procedures [29]. A hanning windows ( $dk=1.0 \text{ \AA}^{-1}$ ) was used to separate the EXAFS contributions from different coordination shells. Furthermore, the quantitative curve-fittings were performed in the R-space with a Fourier transform k-space range of 2.5–11.8  $\text{\AA}^{-1}$  according to the module ARTEMIS of

IFEFFIT. The overall amplitude reduction factor S02, which was derived by fitting the data of Co foil, was fixed to the best-fit value of 0.75 during the curve-fitting process.

## 2.4. Evaluation of the catalytic activity

TC, several antibiotics and dyes were chosen to be typical organic pollutants for catalytic degradation experiment. Normally, 0.1 g P-PCaCo was immersed in 100 mL TC solution (10 mg/L) and stirred 30 min to achieve adsorption equilibrium. And negligible concentration changes were found. After that, 20 mg PMS was added with constant stirring while timer was started at the meantime. At given time, 1 mL solution was taken out for UV-vis spectroscopic characterization. The concentration of TC was represented by peak intensity at about 357 nm. For application tests, RhB, MB, MN, OFX, and STZ were also represented by UV-vis peak intensity at about 552, 665, 318, 290, and 285 nm. For cycling tests, the modified fabric was squeezed and put into a new reaction beaker after each cycle.

## 2.5. Computational methods

Structure of the catalyst was determined by X-ray photoelectron spectroscopy (XPS) and X-ray absorption fine structure (XAFS) experiments, and the simplified model was denoted as AO-CaCo. For better explanation, models of Co<sup>2+</sup> in aqueous solution (denoted as [Co(H<sub>2</sub>O)<sub>6</sub>]<sup>2+</sup>) and Co<sup>2+</sup> complexed by amidoxime group (denoted as AO-Co) were established. Ca<sup>2+</sup> and Co<sup>2+</sup> are both sp<sup>3</sup>d<sup>2</sup> hybridized and bind water in a regular octahedral configuration under acidic or neutral conditions [30,31]. All DFT calculations except specially mentioned used hybrid B3LYP-D3(BJ) exchange-correlation functional with the def2-TZVP basis set for all atoms [32,33]. No imaginary frequency was found with adopting tight convergence criteria meanwhile. All calculations were carried out using Gaussian 09 revision D.01 [34]. The frontier molecular orbitals and evaluation of molecular electrostatic potential (ESP) were analyzed by Multiwfns version 3.8 and VMD version 1.9.3 [35–38].

## 3. Results and discussion

### 3.1. Design of P-PCaCo

The synthesis process of the material is shown in Scheme 1. Polyethylene/polyethylene terephthalate nonwoven fabric (PE/PET NWF) comprises a polyethylene (PE) outer layer with a polyethylene terephthalate (PET) inner layer, and is affordable and readily available. The inner PET layer makes it smooth and robust, while the outer PE layer can be easily modified. Free radicals, which can initiate the graft polymerization, are conveniently produced on this kind of fabric under electron beam irradiation. The well-established RIGP technique enables a strong connection between the substrate and functional layers [39,40]. The PE/PET NWF from which polyacrylonitrile has been grafted was denoted as P-PAN, and as P-PAO after the amidoxime reaction. Amidoxime is an easily-produced chelating group with excellent adsorption capacity. Meanwhile, its high electron cloud density is not only beneficial for attracting organic pollutant molecules, but may also promote the activity of catalysts through electron conduction. Therefore, using amidoxime groups to firmly adsorb typical high-efficiency catalyst, such as Co<sup>2+</sup>, could enable combination of the catalyst and the large-scale substrates. However, excessive chelation can have a negative effect by poisoning the catalyst. And the reducibility of amidoxime groups might lead to the formation of Co<sup>0</sup>, which has a high propensity for aggregation and low activity [3]. Herein, Ca<sup>2+</sup> was introduced to adjust the complex structure, which protects cobalt from reduction and exposes the empty orbitals of Co<sup>2+</sup> to be bound by PMS in the meantime. Ca<sup>2+</sup> can also increase the positive electrostatic potential, which attracts PMS. On the other hand, electro-migration between calcium and cobalt through

amidoxime groups also enhances the catalytic activity. Thus, the introduction of amidoxime groups to adsorb  $\text{Ca}^{2+}$  and  $\text{Co}^{2+}$  produces catalysts with high stability, high atom-utilization efficiency, and high reaction activity.

### 3.2. Physico-chemical properties of the modified fibers

The micro-morphologies and compositions of the pristine and modified nonwoven fabric were studied via scanning electron microscopy (SEM) and energy dispersive spectrometry (EDS), and the results are shown in Fig. 1a. In all samples, the nonwoven fabrics show a random and similar three-dimensional network construction caused of irregular and uniform fibers, which could ensure enough specific surface and liquid flux. The only noticeable change in the surface morphologies is the fiber diameter, which increases from 19  $\mu\text{m}$  for pristine PE/PET NWF to 25  $\mu\text{m}$  for P-PAN. This suggests that the grafting layer, which is primarily polyacrylonitrile, is 3.0  $\mu\text{m}$  thick. Moreover, it seems that changes of micro-morphologies after amidoxime reaction or adsorption are negligible. EDS maps of P-PCaCo verify the presence of Ca and Co. Specifically, the signals of Ca and Co are distributed along the fiber, which indicates a favorable and uniform adsorption of metal ions onto the fabrics without any visible nanoparticles. X-ray diffraction (XRD) patterns as shown in Fig. 1b also confirm that there is no aggregation of Co after chemical modification and adsorption. The prominent peaks in

the low-angle region can be attributed to crystallization of the substrate, as PE and especially PET crystallizes facilely with a large-size lattice arrangement. These broad peaks are typical of polymers, and the sharp peak at 24° is a common PET signal. However, as the amidoxime group is reductive, it can cause many metals, including cobalt, to aggregate and form nanoparticles [41]. Here XRD confirms that cobalt exists in ionic form, and shows no signal of crystal, which can be attributed to the protection of  $\text{Ca}^{2+}$ , and this would be discussed furtherly.

Attenuated total reflection infrared spectra (ATR-IR), X-ray photoelectron spectroscopy (XPS) and X-ray absorption fine structure (XAFS) were used to analyze the chemical structures of the complex on the polymeric substrates. ATR-IR spectra as shown in Fig. 1c confirms the successful preparation of pristine PE/PET NWF, P-PAN, P-PAO and P-PCaCo. The peaks centered at 1714  $\text{cm}^{-1}$  are attributed to the  $-\text{C}=\text{O}$  stretching vibrations of the PET chains, while the peaks at 2849 and 2916  $\text{cm}^{-1}$  are leaded by the  $-\text{CH}_2-$  symmetrical and anti-symmetrical stretching vibrations, respectively, which primarily originate from the PE chains. It is worth noting that PET also exhibits  $-\text{CH}_2-$  stretching vibrations, but this signal is very weak owing to the rigidity of its chain. These peaks are observed in all the spectra and confirm the PE/PET structure of the substrate. The peaks at 2243  $\text{cm}^{-1}$  are characteristic bands of the nitrile group and disappear after the amidoxime reaction, indicating the successful grafting of polyacrylonitrile. The peaks at 933, 1386, 1646 and 3200–3500  $\text{cm}^{-1}$  are assigned to the  $-\text{N}-\text{O}-$ ,  $-\text{C}-\text{O}-$ ,

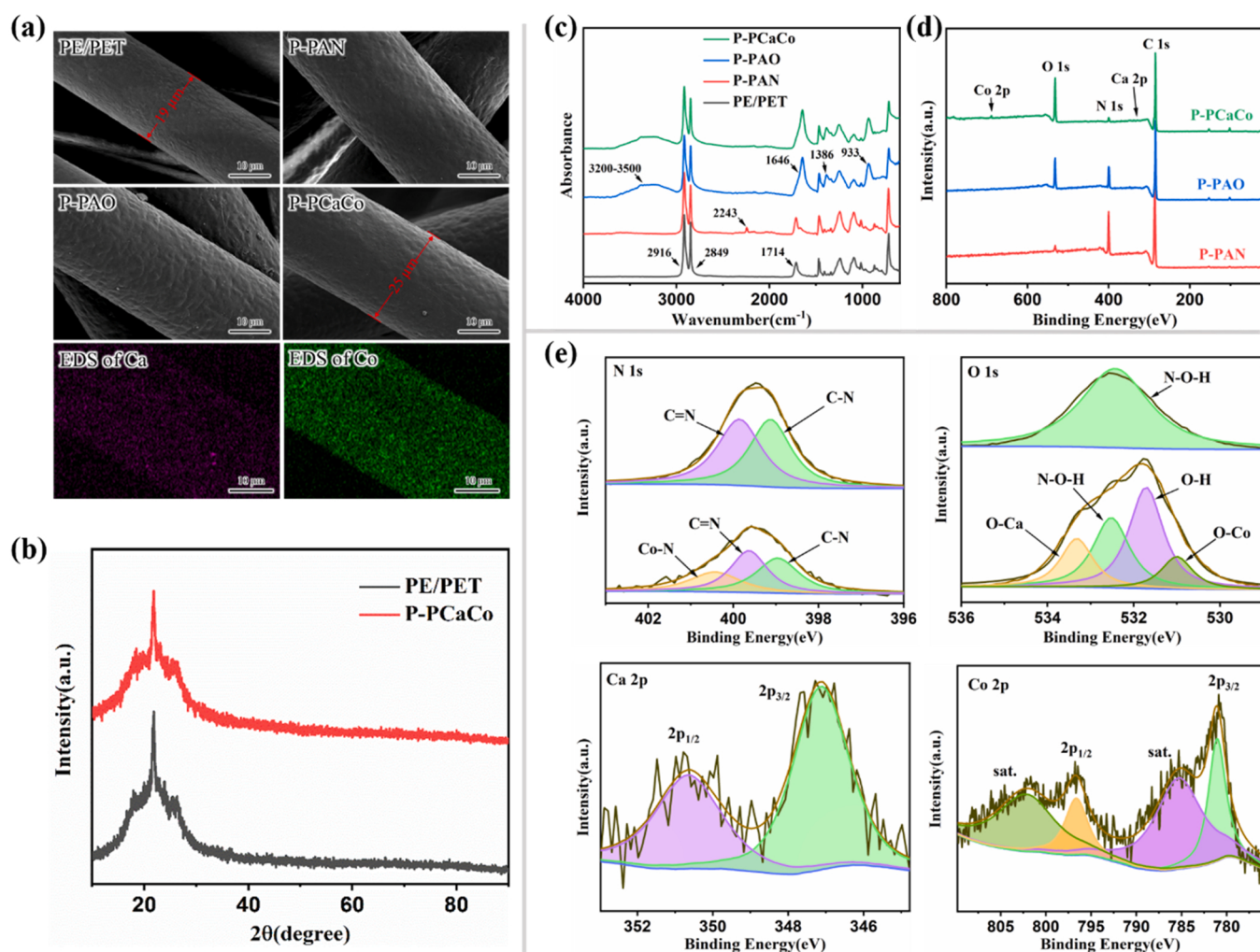


**Fig. 1.** (a) SEM images of PE/PET, P-PAN, P-PAO, and P-PCaCo, EDS maps of Ca and Co on the P-PCaCo surface. (b) XRD patterns of PE/PET and P-PCaCo. (c) ATR-IR spectra of PE/PET NWF, P-PAN, P-PAO, and P-PCaCo. (d) Wide XPS spectra of P-PAN, P-PAO, and P-PCaCo. (e) N 1 s and O 1 s core-level spectra of P-PAO and P-PCaCo, Ca 2p and Co 2p core-level spectra of P-PCaCo.

$\text{-C}\equiv\text{N}$ -,  $\text{-O-H}$ , and  $\text{-N-H}$  stretching vibrations, respectively, and suggest the existence of polyamidoxime. Further characterization of the chemical structure and elemental composition was performed using XPS, as shown in Fig. 1d. The peaks of C 1 s, N 1 s and O 1 s appear on each curve, which confirms the basic structure of the substrate. However, the N 1 s signal decreases while the O 1 s signal increases, when moving from P-PAN to P-PCaCo, which may be due to the amidoxime reaction and complexing process, respectively. After adsorption, the multiple peaks near 790 eV and 350 eV indicate the present of Ca and Co [42,43]. Fig. 1e shows more detailed views of the N 1 s, O 1 s, Ca 2p and Co 2p spectra. Broadening of the N 1 s and O 1 s peaks is caused by changes in the chemical environment due to adsorption. The new O-H signal that appears in the O 1 s spectrum might originate from water molecules bound to the metal ions. Ca 2p and Co 2p spectra confirm that these ions exist as divalent ions. It should be noted that the bond N-Ca is weak and would result in peaks located at low binding energies below 346 eV [44, 45]. Negligible signals are observed in this region, indicating that  $\text{Ca}^{2+}$  is complexed only by oxygen.  $\text{Ca}^{2+}$  may have been chelated by the oxygen atoms of several amidoxime groups and water molecules.

The XAFS results are also consistent with the above discussion. The fine structure and oxidation state of the Co ions are shown in the x-ray absorption near-edge (XANES) and extended x-ray absorption fine-structure (EXAFS) spectra in Fig. 2. The peak near 7730 eV shows that the valence state of Co remains +2 rather than +3. In Fig. 2b, the Fourier transform extended XAFS exhibits a peak near  $1.5 \text{ \AA}$ , which is assigned to the contribution of the Co-O and Co-N first shells. Compared with the CoO and  $\text{Co}_2\text{O}_3$  spectra in the figure, the peaks at 2 and  $2.5 \text{ \AA}$  in the P-PCaCo spectrum are several times weaker, indicating that no oxide is present. This confirms the excellent dispersion of Co, which is

consistent with the results of XPS and XRD. The ratios of Co:O and Co:N are approximately 4:2, as shown in Table S1. If the Co ions are fully chelated by the amidoxime groups, the Co:N ratio should be higher than the Co:O ratio. By analyzing the bond length and complexation number, it was determined that Co is complexed by the two amidoxime N atoms and four water molecules. Fig. 2d illustrates the proposed coordination structure of Co, which is also supported by the DFT calculation results.

### 3.3. Catalytic performance of P-PCaCo

The PMS activation performance of the P-PCaCo catalyst was assessed using the degradation of TC, a typical organic contaminant in industrial wastewater treatment. A UV-vis spectrophotometer was utilized to detect the concentration of TC, which was checked by HPLC experiments, as shown in Fig. S1. Contrasting integration results of UV-Vis and HPLC proves they do the same effect and reach the equilibrium at the same time, as shown in Fig. S2.

Catalysts with different ion ratios were used to confirm the high efficiency of P-PCaCo, as shown in Fig. 3a. Control groups were used to exclude the influence of the amidoxime group. While the certain mass of P-PAO was added, the concentration of TC decreased and quickly reached equilibrium. In fact, amidoxime groups have an adsorption ability, due to its electron-donating double bonds and highly electronegative atoms. When TC is ionized and negatively charged in aqueous solutions, P-PAO would adsorb some TC ions and saturate quickly. This adsorbent group helps organic contaminants move closer to the catalytic sites. Beyond this, P-PAO was immersed in solutions with different  $\text{Ca}^{2+}/\text{Co}^{2+}$  ratios and the highest catalytic performance was observed with a 1:3  $\text{Ca}^{2+}/\text{Co}^{2+}$  ratio. The pH of the metal ion solution is 6.1.

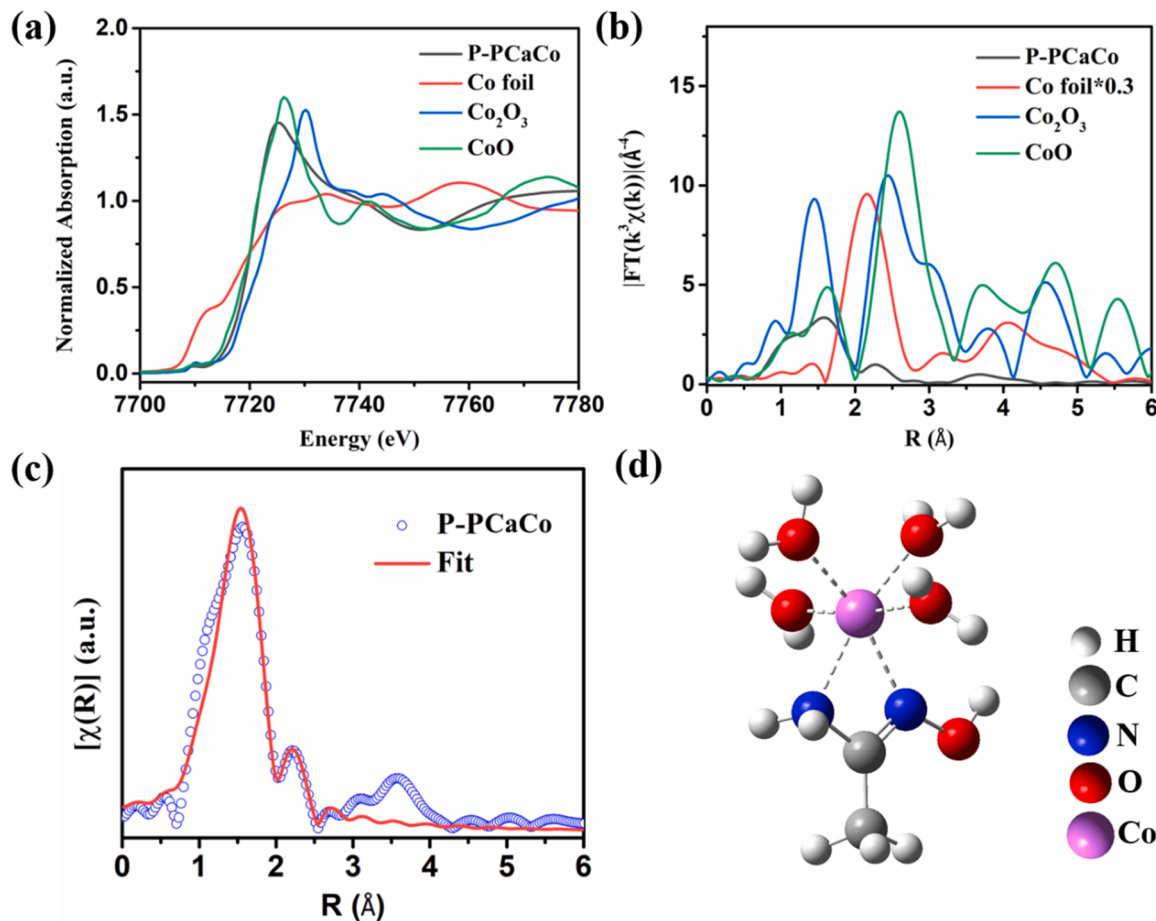
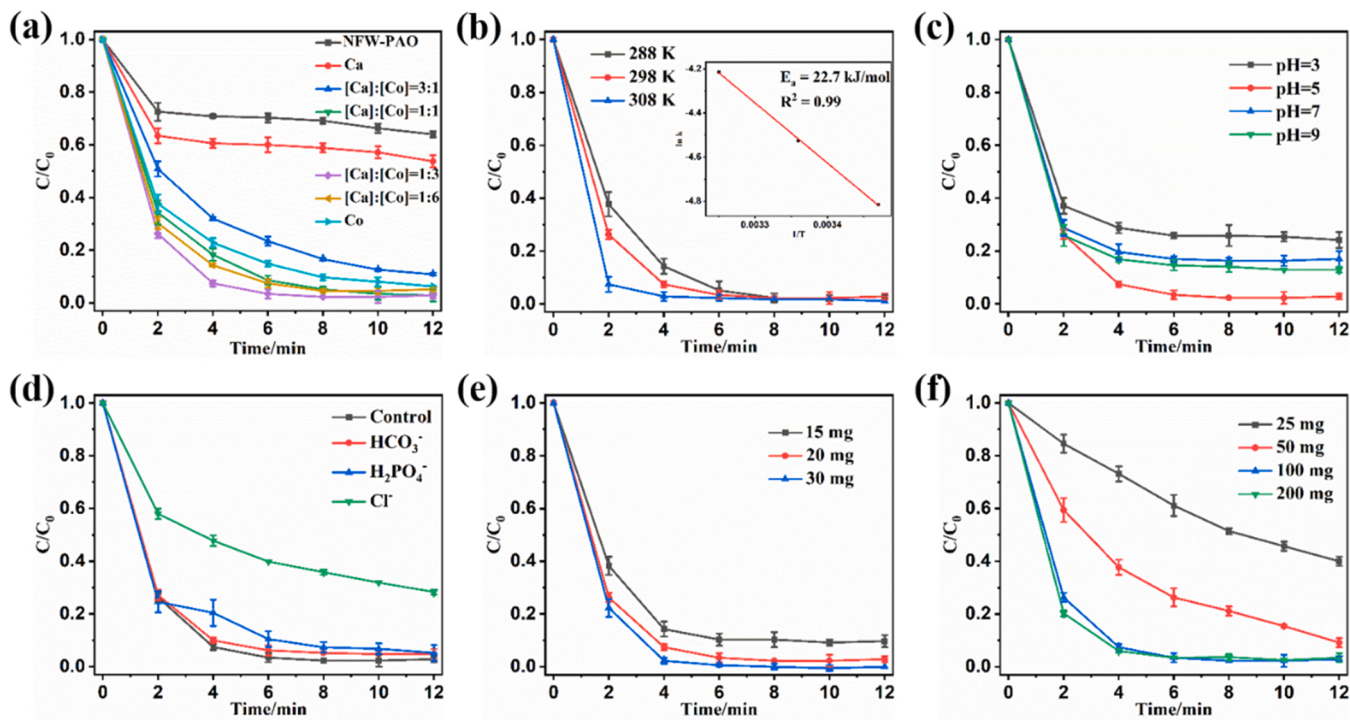


Fig. 2. (a) Co K-edge XANES spectra and (b) R-space EXAFS magnitudes of P-PCaCo, Co foil,  $\text{Co}_2\text{O}_3$ , and CoO. (c) The EXAFS fitting curves of P-PCaCo. (d) The coordination structure of Co.



**Fig. 3.** (a) TC removal efficiency under different catalyst. Influences of (b) temperature, (c) pH, (d) common anions, (e) the dosage of PMS, and (f) the dosage of catalyst. ( $[TC] = 10 \text{ mg} \cdot \text{L}^{-1}$ , catalyst dosage =  $1 \text{ g} \cdot \text{L}^{-1}$ ,  $[\text{PMS}] = 0.2 \text{ g} \cdot \text{L}^{-1}$ ,  $T = 298 \text{ K}$ , initial solution pH = 5.0).

Under this condition, TC removal ratio achieved 97% within 8 min. This indicated that amidoxime-modified fabrics with either  $\text{Ca}^{2+}$  or  $\text{Co}^{2+}$  adsorbed were insufficient catalysts, as the bimetallic synergistic catalyst produced the greatest results.  $\text{Ca}^{2+}$  has poor catalyst ability, but it could function as a co-catalyst to promote the performance of  $\text{Co}^{2+}$ . It is well known that  $\text{Co}^{2+}$  has a relatively good catalytic performance, so additional experiments were designed to explore whether other ions could act as a co-catalyst. The results obtained using several other metal ions directly demonstrate the failure of these ions, as shown in Table S2. Inductively coupled plasma optical emission spectroscopy (ICP-OES) results show that the adsorption capacity of P-PAO is 12.6 mg/g for  $\text{Ca}^{2+}$  and 53.2 mg/g for  $\text{Co}^{2+}$ , which corresponds to an actual mole ratio of approximately 1:4 for  $\text{Ca}^{2+}/\text{Co}^{2+}$ . Same order of magnitude ensures this kind of co-catalyst could work efficiently while other metal ions usually are toxic, expensive, or have a very different adsorption constant. These results demonstrate that  $\text{Ca}^{2+}$  is the best choice and could improve the performance of the catalyst while reducing the cost and amount of cobalt required.

Kinetic studies were used to quantify the enhancement gained by using a co-catalyst system. The kinetics can be simplified to a pseudo first-order equation that depends only on the TC concentration:

$$C_t = C_0 \exp(-kt) \quad (2)$$

The apparent rate constant ( $k$ ) of P-PCaCo is  $0.244 \text{ min}^{-1}$  while it is nearly twice as large as  $k$  of P-PCo which is  $0.138 \text{ min}^{-1}$ . Intuitively, the P-PCo reaction had not reached equilibrium after 12 min, while the P-PCaCo reaction was complete after 6 min.

Studies of catalytic performance under different experimental conditions, as shown in Fig. 3b-3d, were used to evaluate the influences of temperature, pH and common ions. When the temperature is increased from 288 K to 308 K in increments of 10 K, the TC degradation efficiency has a certain improvement, as shown in Fig. 3b. The catalyst reduces the activation energy ( $E_a$ ), while the higher temperature provides more opportunities for the molecules to overcome the reaction barrier. In other words, the catalyst reduces the activation energy which decreases the effect of the temperature. The reaction rate increases with

higher temperatures, while retaining the same reaction endpoint. The Arrhenius equation was used to quantify the effect of temperature:

$$\ln k = \ln k_0 - \frac{E_a}{R} \frac{1}{T} \quad (3)$$

$T$  is the reaction temperature (K),  $R$  is the universal gas constant ( $8.314 \text{ J mol}^{-1} \text{ K}^{-1}$ ), and  $k$  represents different rate constant ( $\text{s}^{-1}$ ). By plotting  $\ln k$  against  $1/T$ , an  $E_a$  value of  $22.7 \text{ kJ/mol}$  was calculated. This value is relatively low and indicates an excellent catalytic effect. Overall, the temperature had a small effect on the catalytic degradation reaction, indicating that P-PCaCo could work efficiently at ambient temperature (Table S3).

Furthermore, the effect of pH was also studied. The pH of the pristine TC solution without any adjustment was about 5.0. The speciation of TC at various pH is shown in Table S4. When pH is below 3, TC is positive charged, which is harmful for approaching the positive charged catalyst. But industrial wastewater is rarely so concentrated that it would have such a low pH [46]. On the other hand, TC would begin changing its chemical conjugation structure when pH is above 7 [47]. Various literatures show that ability of cobalt-based catalysts decay rapidly when the pH is too high [3, 48, 49]. But as shown in Fig. 3c, all curves reach equilibrium within 6 min, indicating that the catalyst could maintain its efficiency under a broaden pH range. However, percentage of degradation at different pH are not completely the same. As shown in Fig. S4, negative charged TC would have a smaller peak at 357 nm in UV-vis spectra. And a smaller initial peak brings a smaller percentage of degradation. In this system, pH appears to have more of an impact on the degradation process than the catalytic reaction. Whatever, P-PCaCo exhibits good catalytic activity over a considerable pH range (3.0–9.0), which is much wider than that required for the Fenton reaction, who is effective only under weak acidic pH conditions.

Considering the complexity of sewage composition, the effect of common anions must be evaluated. In practical applications, wastewater with TC always contains some common anions, such as  $\text{HCO}_3^-$ ,  $\text{H}_2\text{PO}_4^-$ , and  $\text{Cl}^-$ . These anions that arise from the preparation of TC may influence the degradation process and pH of the solution. As shown in Fig. 3d,

with the exception of  $\text{Cl}^-$ , degradation is rarely slowed down in the presence of these anions, which means these common anions have a negligible influence.  $\text{HCO}_3^-$  and  $\text{H}_2\text{PO}_4^-$  are typical buffer agents and the small differences observed in the results may be due to the change in pH rather than the influence of the anions. In contrast, radicals could be slowly transferred to  $\text{Cl}^-$ , and lose their degradative properties. And chloride salts often contain trace amounts of other halide ions and these trace ions can greatly accelerate this transfer process [50].

The dosage of PMS also plays an important role in determining the concentration of radicals. As shown in Fig. 3e, when the PMS concentration is decreased from 0.2 g/L to 0.15 g/L, the reaction rate decreases and TC degradation is less than 90%. However, there is minimal improvement when the PMS concentration is increased from 0.2 g/L to 0.3 g/L. These results show that a concentration of 0.2 g/L is optimal as it delivers a complete reaction at a relatively fast rate. The effect of catalyst dosage gradually saturated, as shown in Fig. 3f. When the dosage is less than 100 mg, there is a significant impact, but at dosages above 100 mg, there is little, which may be caused by the system volume limit and reactant concentration. In the case when the catalytic effect is saturated, the improvement in reaction rate by adding more catalyst rapidly disappears.

In order to verify the impact of pollutants on the degradation rate, we carried out degradation experiments at different concentrations of pollutions, as shown in Fig. S5. The higher concentration seems to need more time to reach the reaction equilibration. The higher TC concentration is, the more possibility of reacting with TC there will be, resulting in increasing the utilization rate of ROS. Thus, a fixed dosage of PMS

tends to degrade more TC when increasing the TC concentration. And the curve flattens more slowly when with a higher degradation efficiency. But the degradation efficiency has little changes when TC concentration is lower than 10 mg/L. In this case, 10 mg/L of TC was chosen to be a general experiment condition.

### 3.4. Reaction mechanism

Investigation the ROS might contribute to understand the specific process of the reaction. Sulfate radicals ( $\text{SO}_4^{\cdot-}$ ), hydroxyl radicals ( $\cdot\text{OH}$ ), and singlet oxygen ( ${}^1\text{O}_2$ ) are three possible ROS that have been reported in PMS activating experiments [3]. The radical quenching method was used to prove the kind of ROS. L-histidine was used for scavenging  ${}^1\text{O}_2$ , tertiary butyl alcohol (TBA) was chosen to eliminate  $\cdot\text{OH}$ , and methanol could wipe out the free radicals mentioned. Fig. 4a shows that all three scavenging reagents slow down the reaction obviously. These experiments indicated that all three ROS might be effective, and every kind of them would influence the final effect.

To further confirm the presence of ROS, EPR analysis, as shown in Fig. 4b and 4c, was performed. 5, 5-Dimethyl-1-pyrroline N-oxide (DMPO) and 2,2,6,6-tetramethyl-4-piperidone (TEMP), which are common radical trappers, were used to detect free radicals and singlet oxygen, respectively. No obviously signals are observed when the radical trappers were added to PMS solutions. However, strong signals appear when the catalyst was also added, which imply that free radicals and  ${}^1\text{O}_2$  are produced. In detail, EPR signals in Fig. 4c correspond to DMPO- $\text{SO}_4^{\cdot-}$  ( $\alpha^N = 13.2 \text{ G}$ ,  $\alpha^H = 9.6 \text{ G}$ ,  $\alpha^H = 1.5 \text{ G}$ , and  $\alpha^H = 0.8 \text{ G}$ ) and

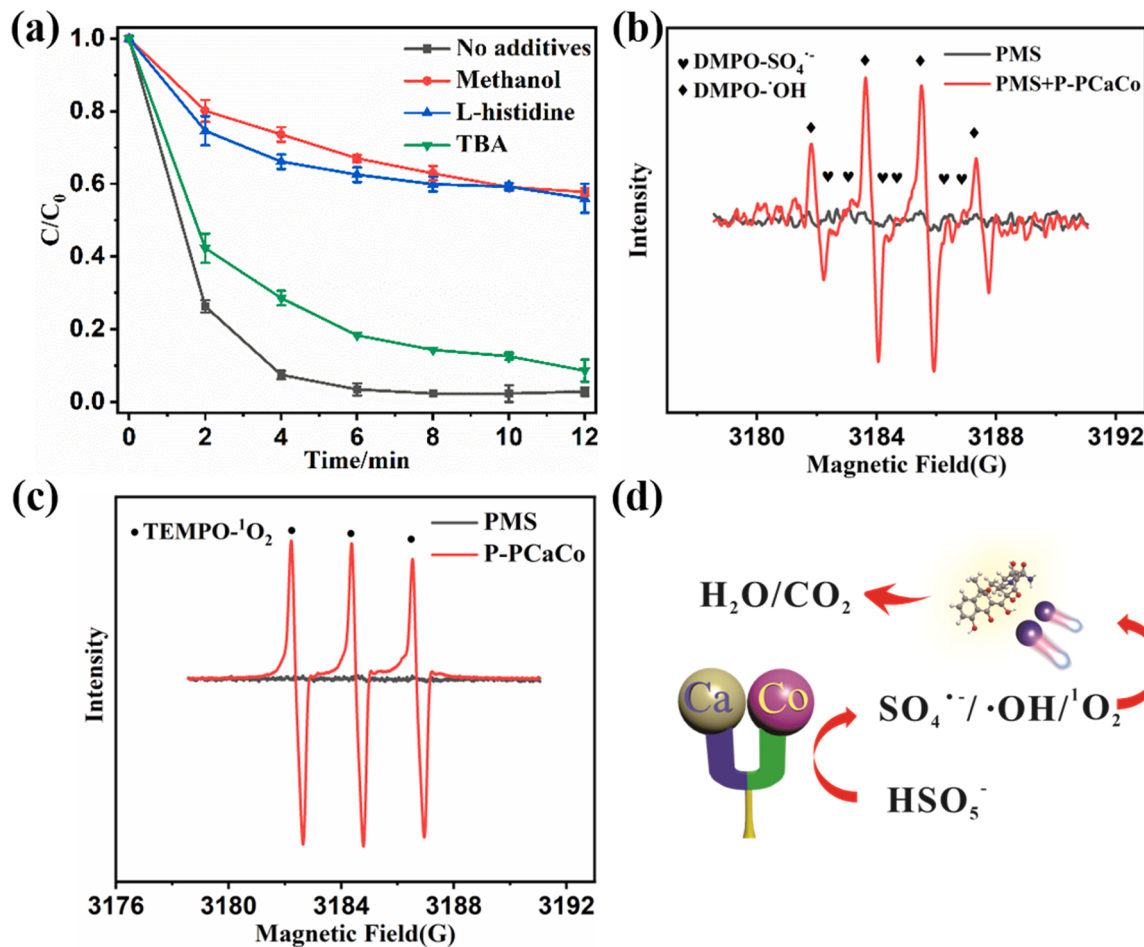
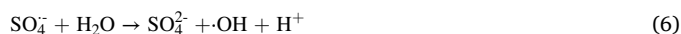


Fig. 4. (a) Effects of various radical scavengers on the TC degradation ([methanol] = 0.5 M, [L-histidine] = 0.5 M, and [TBA] = 0.5 M). EPR spectra of the P-PCaCo/PMS system: (b) DMPO- $\cdot\text{OH}$ , DMPO- $\text{SO}_4^{\cdot-}$  and (c) TEMP- ${}^1\text{O}_2$  ([TC] = 10 mg•L<sup>-1</sup>, catalyst dosage = 1 g•L<sup>-1</sup>, [PMS] = 0.2 g•L<sup>-1</sup>, T = 298 K, initial solution pH = 5.0). (d) Proposed mechanism of P-PCaCo on AOPs reactions.

DMPO-OH ( $\alpha^N = \alpha^H = 13.2$  G) support the existence of  $\text{SO}_4^\cdot$  and prove the presence of  $\cdot\text{OH}$ , while the triplet signal with an integral area ratio of 1:1:1 in Fig. 4c indicates that  ${}^1\text{O}_2$  is present. Overall, the P-PCaCo catalyzing activity practically produces ROS including  $\text{SO}_4^\cdot$ ,  $\cdot\text{OH}$  and  ${}^1\text{O}_2$ . A possible process is illustrated by Fig. 4d. The formation of ROS is based on the following reactions (Eqs. (4)–(7)) [3,25,26]:



Sulfate radicals can be converted to  $\cdot\text{OH}$ . As the weakly acidic environment is not conducive to this transformation, ROS scavenging experiments proves that hydroxyl radicals have less effects than the other radicals. There should be roughly equal amounts of  $\text{SO}_4^\cdot$  and  $\text{SO}_5^\cdot$  produced during the catalytic process. As  $\text{SO}_5^\cdot$  was translated to  ${}^1\text{O}_2$  immediately, ROS scavenging experiments demonstrate that the effects of  ${}^1\text{O}_2$  are comparable to those of  $\text{SO}_4^\cdot$  and  $\cdot\text{OH}$ .

Although the XPS and XAFS results have proven that the O atom of the amidoxime complexes  $\text{Ca}^{2+}$  while the two N atoms chelate  $\text{Co}^{2+}$ , density functional theory (DFT) calculations were required to further confirm the structure, as shown in Fig. 5e. The other possible bonding models were precarious and shown as Fig. S6. As discussed in support information, the structure shown in Fig. 5d is the most stable with the lowest energy. In fact,  $\text{Ca}^{2+}$  could be complexed by two or more O atoms on different amidoxime groups, and the true structure in Fig. 5d was used to simplify the calculation. This type of structure provides at least

two benefits. Firstly,  $\text{Ca}^{2+}$  prevents cobalt from aggregation, which might lead to form nanoparticles. Secondly, the coordination of  $\text{Ca}^{2+}$  sterically hinders the further complexation of  $\text{Co}^{2+}$  by amidoxime groups. Excessive complexation of  $\text{Co}^{2+}$  reduces the number of catalytic sites and impedes the reaction. Conversely, positively charged  $\text{Ca}^{2+}$  might increase the hydrophilicity of catalyst and attract negatively charged PMS.

To analyze the improvement in catalytic performance of P-PCaCo, DFT calculations were also performed to calculate  $\text{Co}^{2+}$  in different states. Simplified models of  $\text{Co}^{2+}$  solvated in water (denoted as  $[\text{Co}(\text{H}_2\text{O})_6]^{2+}$ ),  $\text{Co}^{2+}$  complexed by amidoxime group (AO-Co) and  $\text{Ca}^{2+}/\text{Co}^{2+}$  coordinated with amidoxime group (AO-CaCo) were optimized, as shown in Figs. 5a, 5c and 5e. Moreover, appropriate bond lengths and conformations imply a rational structure. Furthermore, the frontier molecular orbitals, which include the highest occupied molecular orbitals (HOMO) and the lowest unoccupied molecular orbitals (LUMO), and the HOMO-LUMO energy difference ( $\Delta E$ ) were shown in Figs. 5b, 5d and 5f. It is significant that  $\Delta E$  decreases from 5.00 eV to 4.29 eV when  $\text{Co}^{2+}$  is complexed by amidoxime group. As it suggests that the conjugated ligand not only provides adsorption sites but also enhances catalytic performance. Additionally,  $\Delta E$  is further reduced to 3.69 eV when  $\text{Ca}^{2+}$  is also complexed.  $\Delta E$  of alpha orbital also drops from 8.62 eV to 6.71 eV, and reaches 5.83 eV (Fig. S7). Although  $\Delta E$  falls observably here, the actual  $\Delta E$  drop would be even more in practical situations due to the multi-adsorption of  $\text{Ca}^{2+}$ .  $\text{Ca}^{2+}$  could act as bridges for amidoxime groups to further expand the conjugation range, leading to a splitting of the energy levels and a further decrease in  $\Delta E$ . Furthermore, the frontier molecular orbitals of P-PCaCo indicates that this structure can bring a precise electron migration. When the catalyst molecular reaches the

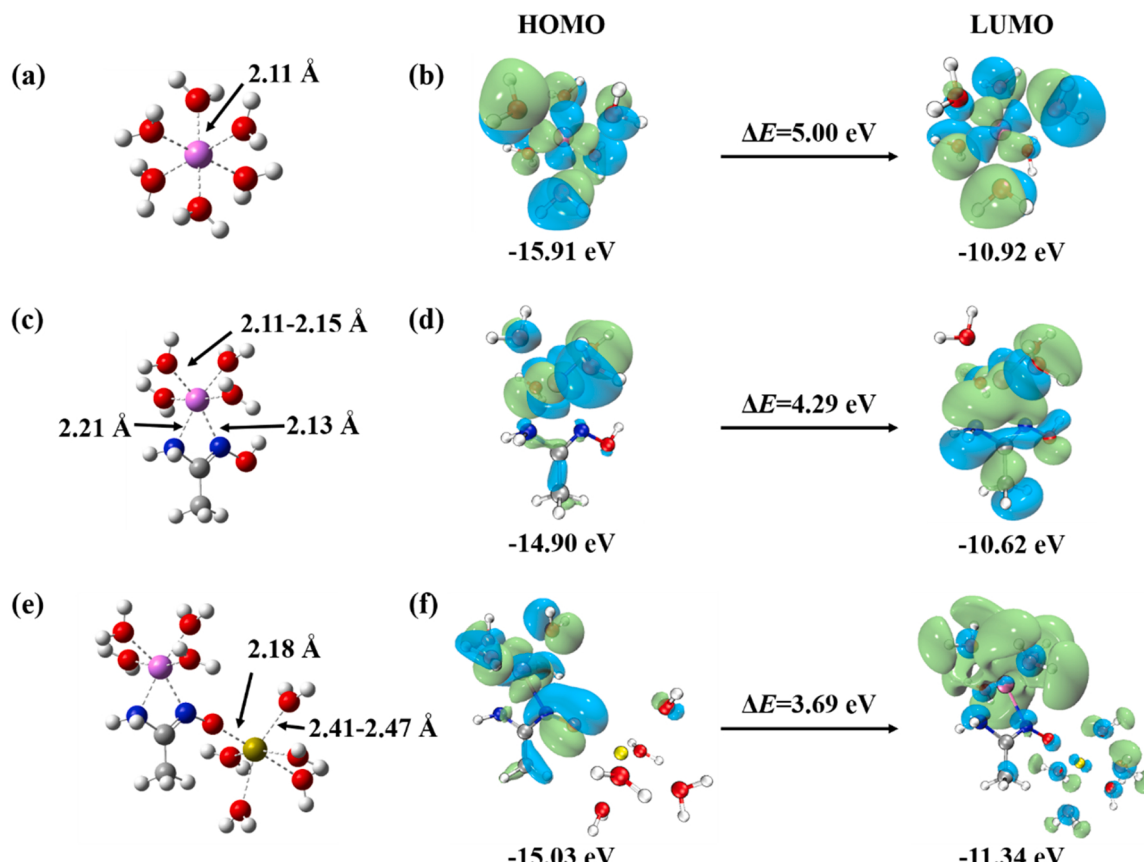


**Fig. 5.** DFT calculations of  $\text{Co}^{2+}$  in different states. (a) The optimized structure and (b) frontier molecular orbitals of  $[\text{Co}(\text{H}_2\text{O})_6]^{2+}$ . (c) The optimized structure and (d) frontier molecular orbitals of AO-Co. (e) The optimized structure and (f) frontier molecular orbitals of AO-CaCo. Each energy level and its difference are shown. Spheres in white, grey, blue, red, yellow and mauve represent H, C, N, O, Ca and Co respectively. Lime and cyan clusters denote positive and negative electron cloud density, which is plotted for iso-values of  $\pm 0.02$  at. units.

excited state, molecular orbitals will be concentrated near Co atom, as shown in Fig. 5e. This electron migration may facilitate the bonding of Co and PMS. On the other hand, the color of the catalyst is brownish black while  $\text{Co}^{2+}$  is shiny red in solution or solid state, as shown in Fig. 7c. The orbits of  $\text{Co}^{2+}$  get closer with the effects of  $\text{Ca}^{2+}$  and amidoxime groups, which result in a drop in the transition energy, influencing the catalysis activity and the color finally. In conclusion, amidoxime groups can reduce HOMO-LUMO energy difference, with  $\text{Ca}^{2+}$  playing a similar role, which result in a high catalytic performance.

Surface charges of catalyst molecules and the catalytic reaction intermediates were analyzed to furtherly confirm the promotion in catalytic process, as shown in Fig. 6. The ESP statistics of AO-CaCo show that the entire molecular surface has very high positive charges, which have a strong attraction to negatively charged PMS ions. There is no negative charge region, so the minimum charge regions have a low reactivity and seems meaningless in this process. The maximum regions of the charge were shown in detail as Fig. 6b. The absolute maximum charge point is located at the surface of Co with a value of 10.29 eV, which implies the most reactive location. It illustrates the charge transfer between  $\text{Ca}^{2+}$  and  $\text{Co}^{2+}$  again.

Based on ESP results, the intermediates and  $\Delta E$  in PMS reaction were calculated as shown in Figs. 6c-6e. The binding of PMS and  $\text{Co}^{2+}$  has a strong kinetic drive, which is the most significant for AO-CaCo. However,  $\Delta E$  of AO-Co is larger than it of  $[\text{Co}(\text{H}_2\text{O})_6]^{2+}$ , which could be due to the negative charges of amidoxime groups. This disadvantage is completely reversed after the introduction of  $\text{Ca}^{2+}$ . These results indicate that P-PCaCo improves the energy levels and charges of  $\text{Co}^{2+}$ , which facilitates the binding and catalytic decomposition of PMS. After the formation of intermediates, the frontier orbital electrons would reach LUMO as shown in Fig. 5 and catalyze PMS. Since such a high positive charge of P-PCaCo could not attract positively charged TC, PMS would break down as reported and form various AOPs, which can react

with organic pollutants[8].

### 3.5. Application tests in practical environments

Stability and reusability are two of the most important parameters for long-term usability and cost-effectiveness. Fig. 7a proves ongoing experiments with five iterations that confirm the reusability of this material. The reaction rate and removal efficiency remained high. SEM and XRD measurements were also carried out for proving the stability, as shown in Fig. S8 and S9. These results indicate there is little change compared with the pristine catalyst, demonstrating that this kind of catalyst can maintain great catalytic ability during cycling uses. In addition, ICP-OES was used to test the ion-leaching rate. The concentration of  $\text{Ca}^{2+}$  and  $\text{Co}^{2+}$  in solution after reaction was 0.45 and 0.55 mg/L respectively, which is negligible compared to the concentration of ions remaining on the catalyst. The concentration of metal ions on the catalyst was 12.6 mg/g for  $\text{Ca}^{2+}$  and 53.2 mg/g for  $\text{Co}^{2+}$ , which corresponds to a solution concentration of 12.6 mg/L for  $\text{Ca}^{2+}$  and 53.2 mg/L for  $\text{Co}^{2+}$ . This level of leached ions is within the limits stipulated in the Chinese integrated wastewater discharge standard (GB8978–1996).

To evaluate the practicality of P-PCaCo, several organic pollutants and solution environments were used. As shown in Fig. 7b, two common dyes and three common antibiotics, Rhodamine B (RhB), methylene blue (MB), metronidazole (MN), ofloxacin (OFX) and sulfathiazole (STZ), were examined. To verify that the organic pollutants were degraded rather than adsorbed, the catalysts were immersed in an alkaline aqueous solution ( $\text{pH} = 12$ ) for 6 h. P-PCaCo exhibited an appropriate removal rate in all groups, indicating that it could be widely applied to the treatment of organic contaminants. The degradation of OFX and STZ are slightly less effective, which might be due to their complex chemical structure and greater demand of PMS. The TOC tests were also carried

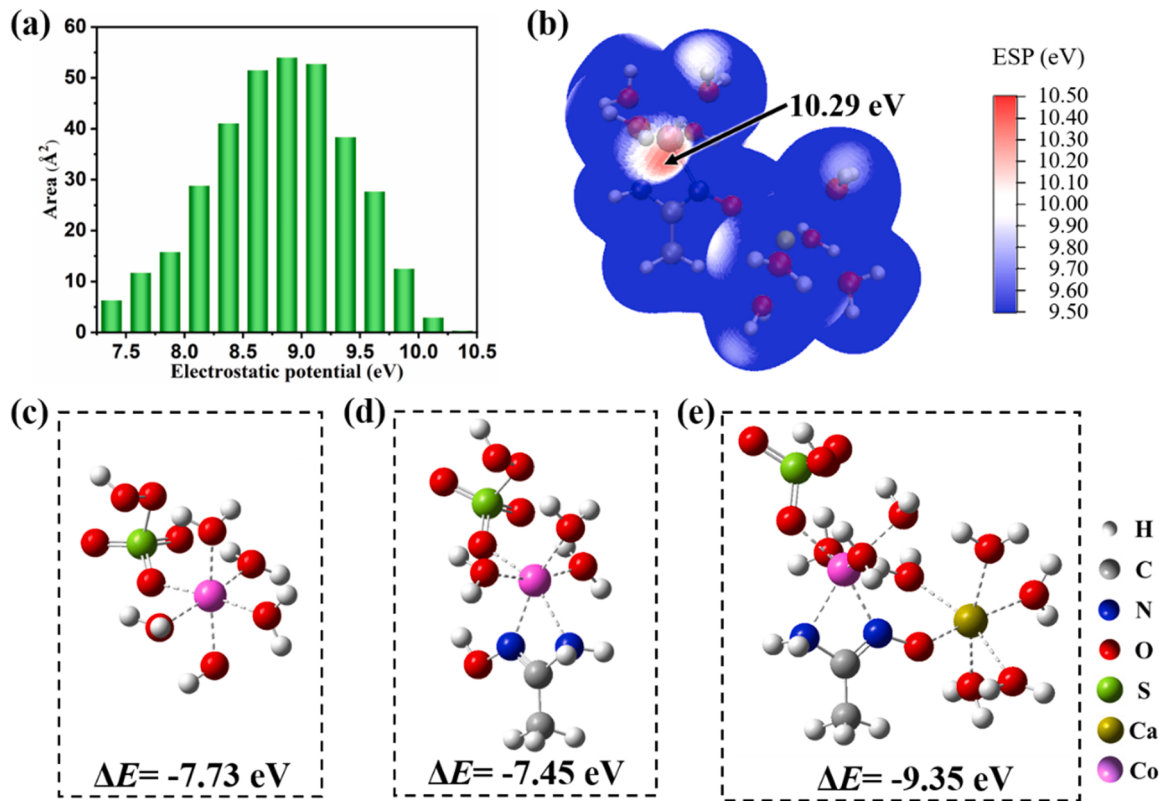


**Fig. 6.** (a) The area percent in each ESP range of AO-CaCo. (b) ESP mapped molecular vdW surface of AO-CaCo (The most charged parts are presented. The molecular conformation is the same as Fig. 5e. The maximum of ESP is labelled by the text.). The intermediates and  $\Delta E$  in PMS reaction with (c)  $[\text{Co}(\text{H}_2\text{O})_6]^{2+}$ , (d) AO-Co, and (e) AO-CaCo.

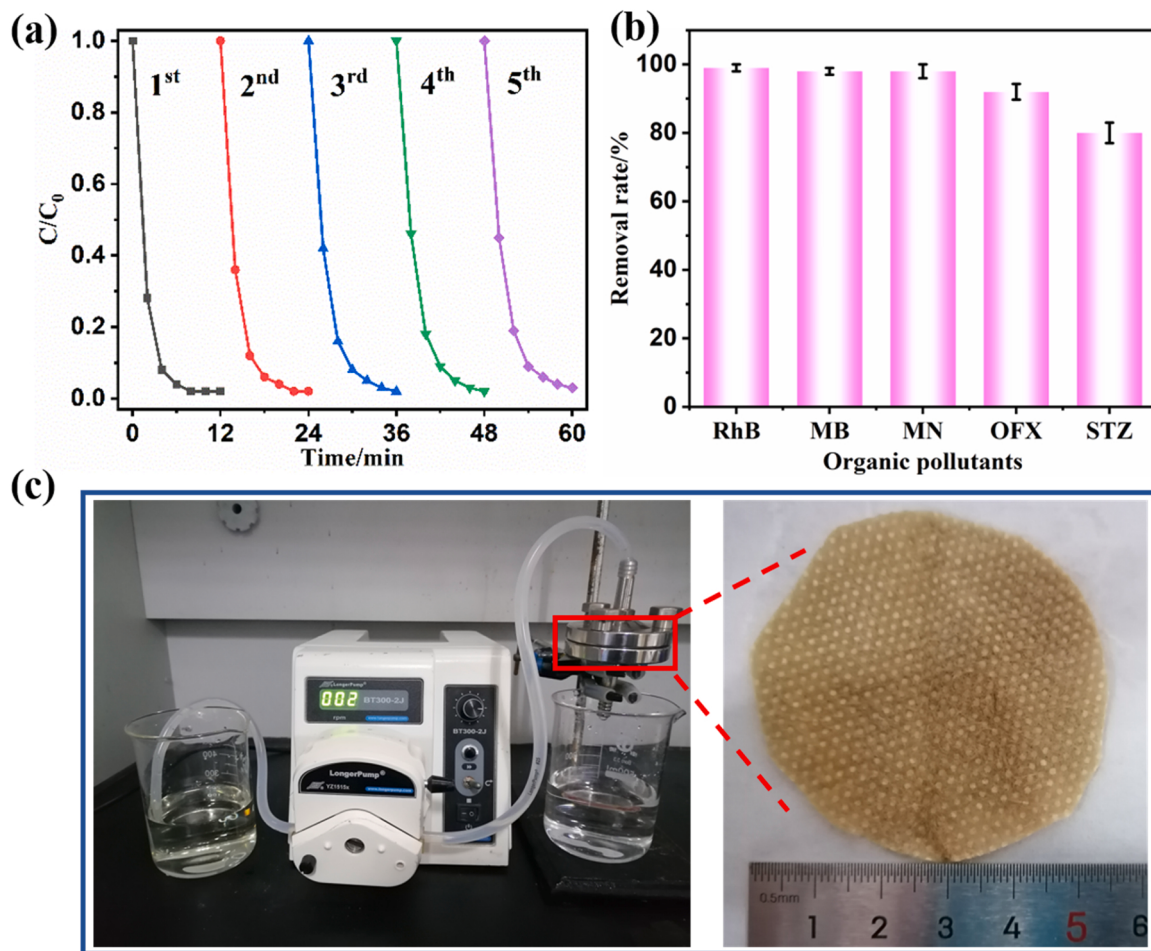


**Fig. 7.** (a) Reusability test on P-PCaCo in terms of TC removal ( $[TC] = 10 \text{ mg}\cdot\text{L}^{-1}$ , catalyst dosage =  $1 \text{ g}\cdot\text{L}^{-1}$ , [PMS] =  $0.2 \text{ g}\cdot\text{L}^{-1}$ ,  $T = 298 \text{ K}$ , initial solution pH = 5.0). (b) Degradation removal rate of different organic pollutants (Organic pollutants concentration =  $10 \text{ mg}\cdot\text{L}^{-1}$ , catalyst dosage =  $1 \text{ g}\cdot\text{L}^{-1}$ , [PMS] =  $0.2 \text{ g}\cdot\text{L}^{-1}$ ,  $T = 298 \text{ K}$ , initial solution pH = 5.0). (c) Device test of P-PCaCo for TC removal ( $[TC] = 30 \text{ mg}\cdot\text{L}^{-1}$ , [PMS] =  $0.6 \text{ g}\cdot\text{L}^{-1}$ ,  $T = 298 \text{ K}$ ), the inset is the digital picture of P-PCaCo.

out for each organic pollution, as shown in Fig. S10. And TOC results give an acceptable degradation consequence. Furthermore, catalytic performance was tested in realistic water conditions as shown in Fig. S11. TC could be degraded within 7 min for tap water and 10 min for wastewater. Tap water may contain  $\text{Cl}^-$  or other minor ions, which could slightly reduce the reaction rate. Additionally, a device test was constructed for practical application as shown in Fig. 7c and Video S1. A piece of P-PCaCo was sandwiched by two flanges and a continuous TC solution was injected using a syringe pump. Colorless and clear water was constantly obtained. In conclusion, P-PCaCo can maintain sufficient efficiency to treat various types of organic pollutions in a realistic environment.

Supplementary material related to this article can be found online at doi:10.1016/j.apcatb.2023.122698.

#### 4. Conclusion

In summary, a new type of PMS catalyst was developed by modifying two metal ions adsorbed on nonwoven fabrics via radiation-induced graft polymerization. This catalyst can be easily prepared and recycled, and shows extremely high catalytic performance. The PE/PET NWF substrate not only provides stability, reusability, and a high specific surface, but also enhances the atomic dispersion degree of catalytic sites via secondary spatial separation in solution.  $\text{Ca}^{2+}$  is used as a co-catalyst to assist the catalytic process by preventing the aggregation of Co and increasing the positive electrostatic potential. In addition,  $\text{Ca}^{2+}$  acts as a

bridge in the conjugated structure, which strengthens the electron migration efficiency and decrease the catalytic reaction energy. The P-PCaCo catalyst can degrade TC within 8 min under different conditions, demonstrating its reliability and versatility. Chemical characterization and radical experiment explained the chemical structure and possible catalytic processes. The structure and high catalytic performance were further explained by theoretical calculations. This study inspires the exploration of similar facile methods to prepare efficient and easily available catalysts for improved AOPs applications to address environmental protection issues.

#### CRediT authorship contribution statement

**Xuanzhi Mao:** Conceptualization, Methodology, Software. **Minglei Wang:** Data curation, Writing. **Ji Li:** Software, Validation. **Maojiang Zhang:** Visualization, Investigation. **Chunlei Dong:** Software, Validation. **Heng Lei:** Software, Validation. **Yulong He:** Software, Validation. **Mingxing Zhang:** Software, Validation. **Zhiqing Ge:** Writing – review & editing. **Rongfang Shen:** Writing – review & editing. **Hongwei Han:** Software, Validation. **Jiangtao Hu:** Supervision. **Guozhong Wu:** Supervision.

#### Declaration of Competing Interest

The authors declare that they have no known competing financial interests or personal relationships that could have appeared to influence

the work reported in this paper.

## Data Availability

Data will be made available on request.

## Acknowledgments

We greatly appreciate supports from National Natural Science Foundation of China (No. 22176194), Talent Introduction Project of Chizhou University (No. RZ2000001341), the Sino-Swiss Science and Technology Cooperation program with ETH Zurich, and the beamline BL14W1 (Shanghai Synchrotron Radiation Facility) for providing the beam time.

## Appendix A. Supporting information

Supplementary data associated with this article can be found in the online version at [doi:10.1016/j.apcatb.2023.122698](https://doi.org/10.1016/j.apcatb.2023.122698).

## References

- [1] S. Reardon, Antibiotic resistance sweeping developing world, *Nature* 509 (2014) 141–142.
- [2] C.-C. Wang, J.-R. Li, X.-L. Lv, Y.-Q. Zhang, G. Guo, Photocatalytic organic pollutants degradation in metal–organic frameworks, *Energy Environ. Sci.* 7 (2014) 2831–2867.
- [3] X. Zheng, X. Niu, D. Zhang, M. Lv, X. Ye, J. Ma, Z. Lin, M. Fu, Metal-based catalysts for persulfate and peroxymonosulfate activation in heterogeneous ways: A review, *Chem. Eng. J.* 429 (2022), 132323.
- [4] L. Ji, W. Chen, L. Duan, D. Zhu, Mechanisms for strong adsorption of tetracycline on carbon nanotubes: a comparative study using activated carbon and graphite as adsorbents, *Environ. Sci. Technol.* 43 (2009) 2322–2327.
- [5] X. Li, B. Kang, F. Dong, Z. Zhang, X. Luo, L. Han, J. Huang, Z. Feng, Z. Chen, J. Xu, B. Peng, Z.L. Wang, Enhanced photocatalytic degradation and H<sub>2</sub>/H<sub>2</sub>O<sub>2</sub> production performance of S-pCN/WO<sub>2.72</sub> S-scheme heterojunction with appropriate surface oxygen vacancies, *Nano Energy* 81 (2021), 105671.
- [6] E. Brillas, I. Sires, M.A. Oturan, Electro-Fenton process and related electrochemical technologies based on Fenton's reaction chemistry, *Chem. Rev.* 109 (2009) 6570–6631.
- [7] L. Hu, P. Wang, T. Shen, Q. Wang, X. Wang, P. Xu, Q. Zheng, G. Zhang, The application of microwaves in sulfate radical-based advanced oxidation processes for environmental remediation: A review, *Sci. Total. Environ.* 722 (2020), 137831.
- [8] J. Lee, U. von Gunten, J.H. Kim, Persulfate-based advanced oxidation: critical assessment of opportunities and roadblocks, *Environ. Sci. Technol.* 54 (2020) 3064–3081.
- [9] I.A. Ike, K.G. Linden, J.D. Orbell, M. Duke, Critical review of the science and sustainability of persulphate advanced oxidation processes, *Chem. Eng. J.* 338 (2018) 651–669.
- [10] L. Yang, J. Xue, L. He, L. Wu, Y. Ma, H. Chen, H. Li, P. Peng, Z. Zhang, Review on ultrasound assisted persulfate degradation of organic contaminants in wastewater: Influences, mechanisms and prospective, *Chem. Eng. J.* 378 (2019), 122146.
- [11] C. Zhu, F. Zhu, C. Liu, N. Chen, D. Zhou, G. Fang, J. Gao, Reductive hexachloroethane degradation by S<sub>2</sub>O<sub>8</sub><sup>2-</sup> with thermal activation of persulfate under anaerobic conditions, *Environ. Sci. Technol.* 52 (2018) 8548–8557.
- [12] D. Zhi, Y. Lin, L. Jiang, Y. Zhou, A. Huang, J. Yang, L. Luo, Remediation of persistent organic pollutants in aqueous systems by electrochemical activation of persulfates: a review, *J. Environ. Manag.* 260 (2020), 110125.
- [13] D.L. Ball, J.O. Edwards, The kinetics and mechanism of the decomposition of Caro's Acid. I, *J. Am. Chem. Soc.* 78 (1956) 1125–1129.
- [14] G.P. Anipstakis, D.D. Dionysiou, Radical generation by the interaction of transition metals with common oxidants, *Environ. Sci. Technol.* 38 (2004) 3705–3712.
- [15] Y.-Y. Ahn, H. Bae, H.-I. Kim, S.-H. Kim, J.-H. Kim, S.-G. Lee, J. Lee, Surface-loaded metal nanoparticles for peroxymonosulfate activation: efficiency and mechanism reconnaissance, *Appl. Catal. B* 241 (2019) 561–569.
- [16] F. Xiao, Z. Wang, J. Fan, T. Majima, H. Zhao, G. Zhao, Selective electrocatalytic reduction of oxygen to hydroxyl radicals via 3-electron pathway with FeCo alloy encapsulated carbon aerogel for fast and complete removing pollutants, *Angew. Chem. Int. Ed. Engl.* 60 (2021) 10375–10383.
- [17] J. Cui, L. Li, S. Shao, J. Gao, K. Wang, Z. Yang, S. Zeng, C. Diao, Y. Zhao, C. Hu, Regulating the metal-support interaction: double jump to reach the efficiency apex of the Fe-N<sub>4</sub>-catalyzed fenton-like reaction, *ACS Catal.* (2022) 14954–14963.
- [18] Y. Li, S. Ouyang, H. Xu, X. Wang, Y. Bi, Y. Zhang, J. Ye, Constructing solid-gas-interfacial fenton reaction over alkalinized-C(3)N(4) photocatalyst to achieve apparent quantum yield of 49% at 420 nm, *J. Am. Chem. Soc.* 138 (2016) 13289–13297.
- [19] D. Wang, M. Suo, S. Lai, L. Deng, J. Liu, J. Yang, S. Chen, M.-F. Wu, J.-P. Zou, Photoinduced acceleration of Fe<sup>3+</sup>/Fe<sup>2+</sup> cycle in heterogeneous FeNi-MOFs to boost peroxydisulfate activation for organic pollutant degradation, *Appl. Catal. B* 321 (2023), 122054.
- [20] R. Cheng, K. Dong, L. Liu, C. Ning, P. Chen, X. Peng, D. Liu, Z.L. Wang, Flame-retardant textile-based triboelectric nanogenerators for fire protection applications, *ACS Nano* 14 (2020) 15853–15863.
- [21] H.Y. Erbil, A.L. Demirel, Y. Avci, O. Mert, Transformation of a simple plastic into a superhydrophobic surface, *Science* 299 (2003) 1377–1380.
- [22] Z. Wang, Y. Wang, G. Liu, Rapid and efficient separation of oil from oil-in-water emulsions using a janus cotton fabric, *Angew. Chem. Int. Ed.* 55 (2016) 1291–1294.
- [23] C.L. Zhang, S.H. Yu, Nanoparticles meet electropinning: recent advances and future prospects, *Chem. Soc. Rev.* 43 (2014) 4423–4448.
- [24] M.-w Kim, H. Yoon, T.Y. Ohm, H.S. Jo, S. An, S.K. Choi, H. Park, S.S. Al-Deyab, B. K. Min, M.T. Swihart, S.S. Yoon, Nanotextured cupric oxide nanofibers coated with atomic layer deposited ZnO-TiO<sub>2</sub> as highly efficient photocathodes, *Appl. Catal. B* 201 (2017) 479–485.
- [25] Y. Liu, X. Zhou, M. Wang, M. Zhang, Y. He, Y. Zhang, R. Shen, Y. Zhang, J. Hu, G. Wu, Co<sup>2+</sup> anchored on surface-functionalized PET non-woven fabric and used as high efficiency monoatom-like catalyst for activating Oxone in water, *Sci. Total. Environ.* 699 (2020), 134286.
- [26] M. Wang, Q. Gao, M. Zhang, Y. He, Y. Zhang, R. Shen, J. Hu, G. Wu, Boosting peroxymonosulfate activation via highly active and durable cobalt catalysts, *J. Mater. Chem. A* 9 (2021) 2308–2318.
- [27] L. Mu, M. Wang, F. Jiang, Q. Gao, M. Zhang, Z. Xiong, Y. Li, R. Shen, J. Hu, G. Wu, Boosting Photo-Fenton reactions by amidoxime chelated ferrous iron (Fe(III)) catalyst for highly efficient pollutant control, *Appl. Catal., B* 298 (2021), 120574.
- [28] H.S. Yu, X.J. Wei, J. Li, S.Q. Gu, S. Zhang, L.H. Wang, J.Y. Ma, L.N. Li, Q. Gao, R. Si, F.F. Sun, Y. Wang, F. Song, H.J. Xu, X.H. Yu, Y. Zou, J.Q. Wang, Z. Jiang, Y. Huang, The XAFS beamline of SSRF, *Nucl. Sci. Tech.* 26 (2015), 050102.
- [29] B. Ravel, M. Newville, Athena, artemis, hephaestus: data analysis for X-ray absorption spectroscopy using IFEFFIT, *J. Synchrotron Radiat.* 12 (2005) 537–541.
- [30] L. Zhang, H. Zhang, Z. Ge, X. Yu, Impact of environmental conditions on the sorption behavior of radionuclide 60Co(II) on MnO<sub>2</sub>, *J. Radioanal. Nucl. Chem.* 288 (2010) 537–546.
- [31] H. Zhou, F. Zhu, Y. Zhou, H. Liu, Y. Fang, C. Fang, Ab initio investigation of the micro-species in [CaCl<sub>2</sub>(H<sub>2</sub>O)<sub>n</sub>] = 0–12] and their Raman, *Spectra, J. Clust. Sci.* 29 (2018) 605–616.
- [32] J.P. Boyd, E. Iranian, A. Grohmann, Tetrapodal amidoxime ligands I. Coordination isomerism due to self-complementary dimerization of a pyramidal cobalt(III) coordination module, *Dalton Trans.* 41 (2012) 2477–2485.
- [33] K.J. Bernstein, C.-L. Do-Thanh, D.A. Penchoff, S. Alan Cramer, C.R. Murdock, Z. Lu, R.J. Harrison, J.P. Camden, D.M. Jenkins, The synthesis and spectroscopic characterization of an aromatic uranium amidoxime complex, *Inorg. Chim. Acta* 421 (2014) 374–379.
- [34] G.J. Frisch, H.B. Schlegel, G.E. Scuseria, M.A. Robb, J.R. Cheeseman, G. Scalmani, V. Barone, B. Menzucci, G.A. Petersson, H. Nakatsuji, M. Caricato, X. Li, H.P. Hratchian, A.F. Izmaylov, J. Bloino, G. Zheng, J.L. Sonnenberg, M. Hada, M. Ehara, K. Toyota, R. Fukuda, J. Hasegawa, M. Ishida, T. Nakajima, Y. Honda, O. Kitao, H. Nakai, T. Vreven, J.A. Montgomery, Jr., J.E. Peralta, F. Ogliaro, M. Bearpark, J.J. Heyd, E. Brothers, K.N. Kudin, V.N. Staroverov, T. Keith, R. Kobayashi, J. Normand, K. Raghavachari, A. Rendell, J.C. Burant, S.S. Iyengar, J. Tomasi, M. Cossi, N. Rega, J.M. Millam, M. Klene, J.E. Knox, J.B. Cross, V. Bakken, C. Adamo, J. Jaramillo, R. Gomperts, R.E. Stratmann, O. Yazyev, A.J. Austin, R. Cammi, C. Pomelli, J.W. Ochterski, R.L. Martin, K. Morokuma, V.G. Zakrzewski, G.A. Voth, P. Salvador, J.J. Dannenberg, S. Dapprich, A.D. Daniels, O. Farkas, J.B. Foresman, J. V. Ortiz, J. Cioslowski, and D.J. Fox, Gaussian 09, Revision D.01, Gaussian, Inc., Wallingford CT, (2013).
- [35] T. Lu, F. Chen, Multiwfns: a multifunctional wavefunction analyzer, *J. Comput. Chem.* 33 (2012) 580–592.
- [36] W. Humphrey, A. Dalke, K. Schulten, VMD: visual molecular dynamics, *J. Mol. Graph.* 14 (33–38) (1996) 27–38.
- [37] J. Zhang, T. Lu, Efficient evaluation of electrostatic potential with computerized optimized code, *Phys. Chem. Chem. Phys.* 23 (2021) 20323–20328.
- [38] S. Manzetti, T. Lu, The geometry and electronic structure of Aristolochic acid: possible implications for a frozen resonance, *J. Phys. Org. Chem.* 26 (2013) 473–483.
- [39] V.Y. Kabanov, V.I. Feldman, B.G. Ershov, A.I. Polikarpov, D.P. Kiryukhin, P. Y. Apel, Radiation chemistry of polymers, *High. Energy Chem.* 43 (2009) 1–18.
- [40] S. Aoki, K. Fujiwara, T. Sugo, K. Suzuki, Antimicrobial fabric adsorbed iodine produced by radiation-induced graft polymerization, *Radiat. Phys. Chem.* 84 (2013) 242–245.
- [41] W. Sun, L. Feng, J. Zhang, K. Lin, H. Wang, B. Yan, T. Feng, M. Cao, T. Liu, Y. Yuan, N. Wang, Amidoxime group-anchored single cobalt atoms for anti-biofouling during uranium extraction from seawater, *Adv. Sci.* 9 (2022), e2105008.
- [42] X. Li, X. Huang, S. Xi, S. Miao, J. Ding, W. Cai, S. Liu, X. Yang, H. Yang, J. Gao, J. Wang, Y. Huang, T. Zhang, B. Liu, Single cobalt atoms anchored on porous N-doped graphene with dual reaction sites for efficient fenton-like catalysis, *J. Am. Chem. Soc.* 140 (2018) 12469–12475.
- [43] K.L.S. Castro, R.V. Curti, J.R. Araujo, S.M. Landi, E.H.M. Ferreira, R.S. Neves, A. Kuznetsov, L.A. Sena, B.S. Archanjo, C.A. Achete, Calcium incorporation in graphene oxide particles: a morphological, chemical, electrical, and thermal study, *Thin Solid Films* 610 (2016) 10–18.
- [44] J. Zhu, L. Wang, T. Zhou, Y. Cho, T. Suehiro, T. Takeda, M. Lu, T. Sekiguchi, N. Hiroaki, R.-J. Xie, Moisture-induced degradation and its mechanism of (Sr,Ca)AlSiN<sub>3</sub>:Eu<sup>2+</sup>, a red-color-converter for solid state lighting, *J. Mater. Chem. C* 3 (2015) 3181–3188.

- [45] S. Li, X. Liu, R. Mao, Z. Huang, R. Xie, Red-emission enhancement of the CaAlSiN<sub>3</sub>: Eu<sup>2+</sup> phosphor by partial substitution for Ca<sub>2</sub>N<sub>2</sub> by CaCO<sub>3</sub> and excess calcium source addition, *RSC Adv.* 5 (2015) 76507–76515.
- [46] M.A. Barakat, New trends in removing heavy metals from industrial wastewater, *Arab. J. Chem.* 4 (2011) 361–377.
- [47] L. Hu, Y. Zhang, X. Liu, H. Zhu, J. Wu, Y. Wang, Y. Long, G. Fan, A robust peroxyomonosulfate activator for tetracycline degradation: Mitigating deactivation via stitching N-doped carbon nanotubes with encapsulated Co nanoparticles in bubble-like architectures, *Chem. Eng. J.* 450 (2022), 138219.
- [48] T. Zeng, X. Zhang, S. Wang, H. Niu, Y. Cai, Spatial confinement of a Co<sub>3</sub>O<sub>4</sub> catalyst in hollow metal-organic frameworks as a nanoreactor for improved degradation of organic pollutants, *Environ. Sci. Technol.* 49 (2015) 2350–2357.
- [49] H. Liang, Y.Y. Ting, H. Sun, H.M. Ang, M.O. Tade, S. Wang, Solution combustion synthesis of Co oxide-based catalysts for phenol degradation in aqueous solution, *J. Colloid Interface Sci.* 372 (2012) 58–62.
- [50] Y. Yang, J.J. Pignatello, J. Ma, W.A. Mitch, Comparison of halide impacts on the efficiency of contaminant degradation by sulfate and hydroxyl radical-based advanced oxidation processes (AOPs), *Environ. Sci. Technol.* 48 (2014) 2344–2351.